Contrib Mineral Petrol (1991) 107:358–372

Contributions to Mineralogy and Petrology

Linked fluid and tectonic evolution in the High Himalaya mountains (Nepal)

Anne-Marie Boullier[1], Christian France-Lanord[1], Jean Dubessy[2], Jérôme Adamy[1], and Michel Champenois[1]

[1] Centre de Recherches Pétrographiques et Géochimiques, BP 20, F-54501 Vandoeuvre cedex France
[2] Centre de Recherche sur la Géologie de l'Uranium, BP23, F-54501 Vandoeuvre cedex, France

Received June 7, 1990 / Accepted October 18, 1990

Abstract. Fluid inclusions were studied in a quartz lens from the structurally highest unit of the Himalaya mountains in Nepal from a textural, geometrical, chemical and isotopic point of view. Six types of fluid inclusions were distinguished. One of these types consists of annular inclusions; this shape is attributed to a confining pressure increase in a non-isotropic stress field. Two successive stress fields were deduced from the orientation of the inclusion planes relative to the schistosity. The bulk composition of the fluid was dominated by CO_2 (>84 mol%) and H_2O. The composition remained constant during the whole history of the sample indicating that it was buffered by the carbonaceous host rock and/or that one single fluid was reworked in situ by decrepitation. Stable isotope of fluids and minerals indicate (1) that fluids were buffered by surrounding rocks for O and C and (2) that at least two types of water (metamorphic and meteoric) were involved. Finally, a $P-T-t-\varepsilon-\sigma$ path is proposed for the sample, taking into account the southward thrusting along the Main Central Thrust, the northward tectonic denudation of the Himalaya mountains inducing tectonic burying below the Annapurna Range, and lastly, rapid uplift.

Introduction

In the absence of precise experimental data, the complicated posttrapping changes which may occur in fluid inclusions can only be approached in a qualitative way. There are many evidences that volume changes (necking-down, stretching, etc., e.g. Touret 1977; Roedder 1981) may occur well after the initial formation of an inclusion and that the familiar "constant density condition" may only refer to a late stage of the inclusion history. In order to model the possible changes of fluid inclusions after trapping, experiments had previously been carried out on quartz to simulate uplift, and burial or cooling. In both cases, the shape and the density of the fluid inclusions changed (Pêcher 1981; Pêcher and Boullier 1984; Boullier et al. 1989a; Sterner and Bodnar 1989). Once adequately recognized and understood, these changes may provide very useful information on (P, T, t) paths. Therefore, it is now possible to come back to natural samples and to compare them with the above experimental results.

An extensive sampling program of quartz lenses through the metamorphic pile of the Himalaya was undertaken to study isotopic composition of the fluids percolating through the pile (France-Lanord 1987; France-Lanord et al. 1988). In parallel, a fluid inclusion study was also carried out to place some additional constraints on the composition of fluids during the strain (ε) history and on the (P, T, t, ε) path (Boullier et al. 1989b). It was noted that some of the structurally highest samples show annular fluid inclusions. Such inclusions were also described by Pagel (1975) and Safronov (1965), but without any explanation of that particular shape. Therefore, a detailed study of fluid inclusions (shape, orientation of planes, density and composition) was performed on one of these samples, to place constraints on the geological evolution of the highest part of the Himalaya.

Offprint requests to: A.M. Boullier

Review of experimental reequilibration of fluid inclusions

The first observations and attempts to reproduce experimentally post entrapment changes were made by Lemmlein and Kliya (1954). In recent times two types of experiments have been performed. The first type of experiments was conducted at one atmosphere confining pressure and various temperatures in order to test the behaviour of fluid inclusions in fluorite (Sabouraud 1981), fluorite and sphalerite (Bodnar and Bethke 1984), barite (Ulrich and Bodnar 1988) or quartz (Leroy 1979; Gratier and Jenatton 1984; Bodnar et al. 1989). Upon heating, fluid inclusions generally decrepitate, and internal pressure required to cause decrepitation is a function of the nature of the host mineral and of the size and

shape of fluid inclusions. In the present paper, decrepitation will be restricted to brittle deformation (microcrack) around a fluid inclusion. In experiments at atmospheric pressure, these cracks are not healed and the decrepitated fluid inclusions are empty.

In the second type of experiment, the samples containing fluid inclusions were submitted to high pressure and temperature conditions which departed from the initial isochoric line. Therefore, these experiments simulated uplift (P and T below the initial isochore), and cooling or burial (P and T above the isochore). The earliest experiments were performed on synthetic quartz crystals with primary ($H_2O-NaOH$) fluid inclusions (Pêcher 1981; Pêcher and Boullier 1984; Boullier et al. 1989a). A new technique of synthetic fluid inclusions allowed Sterner and Bodnar (1989) and Bakker and Jansen (1990) to investigate natural systems (e.g.: $H_2O \pm NaCl$ and H_2O+CO_2). Experiments with both starting materials led to the following main common conclusions:
(1) the density of the fluid decreases if overpressure ($\Delta P>0$, ΔP=internal pressure minus confining pressure) occurs within the fluid inclusion or increases if underpressure ($\Delta P<0$) occurs within the fluid inclusion. In both cases, the density of the fluid evolves toward the density corresponding to the experimental P and T conditions.
(2) the shape of the fluid inclusion evolves toward a regular negative crystal shape.

The differences in starting material and in experimental conditions allow complementary conclusions:
(a) high pressure experiments of different durations demonstrate that the change of shape and the change of density are the result of different, but time-dependent processes. The equilibrium aspect ratio of the inclusions is itself pressure dependent (Pêcher and Boullier 1984; Boullier et al. 1989a);
(b) density reequilibration seems to be volume-independent when confining pressure is lower than internal pressure, and volume-dependent when confining pressure is higher than internal pressure (Boullier et al. 1989a; Sterner and Bodnar 1989);
(c) comparison of equal duration experiments with both starting materials indicate that higher temperatures and larger $|\Delta P|$ values enhance the density decrease of fluid inclusions;
(d) the use of $H_2O+NaCl$ synthetic fluid inclusions clearly demonstrates that density variations are not caused by H_2O diffusion, but mainly by volume changes induced by plastic deformation of the host quartz crystal (Sterner and Bodnar 1989). This conclusion is also strongly suggested by dislocations and diffraction contrast on X-ray topographs around fluid inclusions after experiments (Boullier et al. 1989a). Bakker and Jansen (1990) obtain contradictory results for synthetic H_2O+CO_2 synthetic fluid inclusions and suggest that preferential water leakage occurs;
(e) because of the large size (up to 10^6 μm^3) of some fluid inclusions in the synthetic quartz crystals, decrepitation also occurs by internal overpressure (equation of Bodnar et al. 1989). In such cases, a decrepitation cluster of small fluid inclusions results from healing of the cracks by a dissolution-recrystallization process (Lemmlein and Kliya 1954; Smith and Evans 1984). These small fluid inclusions exhibit a narrow range of density, closely matching the experimental P and T conditions (Pêcher and Boullier 1984; Boullier et al. 1989a);
(f) large underpressure in initially low density fluid inclusions is generally accompanied by a characteristic "implosion halo" of small fluid inclusions displaying a large range of Th (temperature of homogenization). These features may aid the inclusionist to recognize such a density increase in natural samples (Sterner and Bodnar 1989). However, only direct measurements of density allow distinction between decrepitation halos (cf Lemmlein and Kliya 1954) and implosion halos (cf Sterner and Bodnar 1989) which share similar morphologies;
(g) finally, Pêcher (1981) produced annular fluid inclusions (Fig. 3d in Pêcher 1981, Fig. 1, this paper) during experiments of short duration performed in a solid medium Griggs apparatus at around 800 MPa confining pressure and 510° C. As indicated by Pêcher, "... stress state might have been irregular and only very approximately isotropic..." due to the pressure medium (fluorite powder). Internal pressure of the fluid inclusions was about 370 MPa, and was therefore far below the confining pressure. Single tubular fluid inclusions were transformed into annular fluid inclusions flattened in the YZ plane (Fig. 1). They are surrounded by a cluster of numerous small fluid inclusions comparable to the implosion halos described by Sterner and Bodnar (1989). This transformation never appeared during the experiments in a gas apparatus at the same P and T conditions under positive or negative ΔP. Therefore, Pêcher (1981) proposed that the annular fluid inclusions are induced y anisotropy of the stress (σ) field.

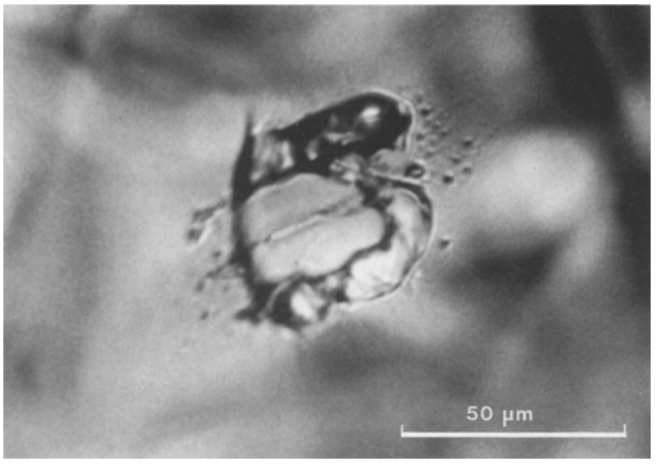

Fig. 1. Photomicrograph of an annular fluid inclusion experimentally produced by Pêcher (1981). The section is perpendicular to the compression axis and is oriented at 45° the to c axis of the synthetic quartz. The fluid inclusion was initially cylindrical. Note the halo of small inclusions around the large one

Geological context

The Himalaya mountains result from a convergent orogeny where crustal shortening and thickening are related to southward thrust-

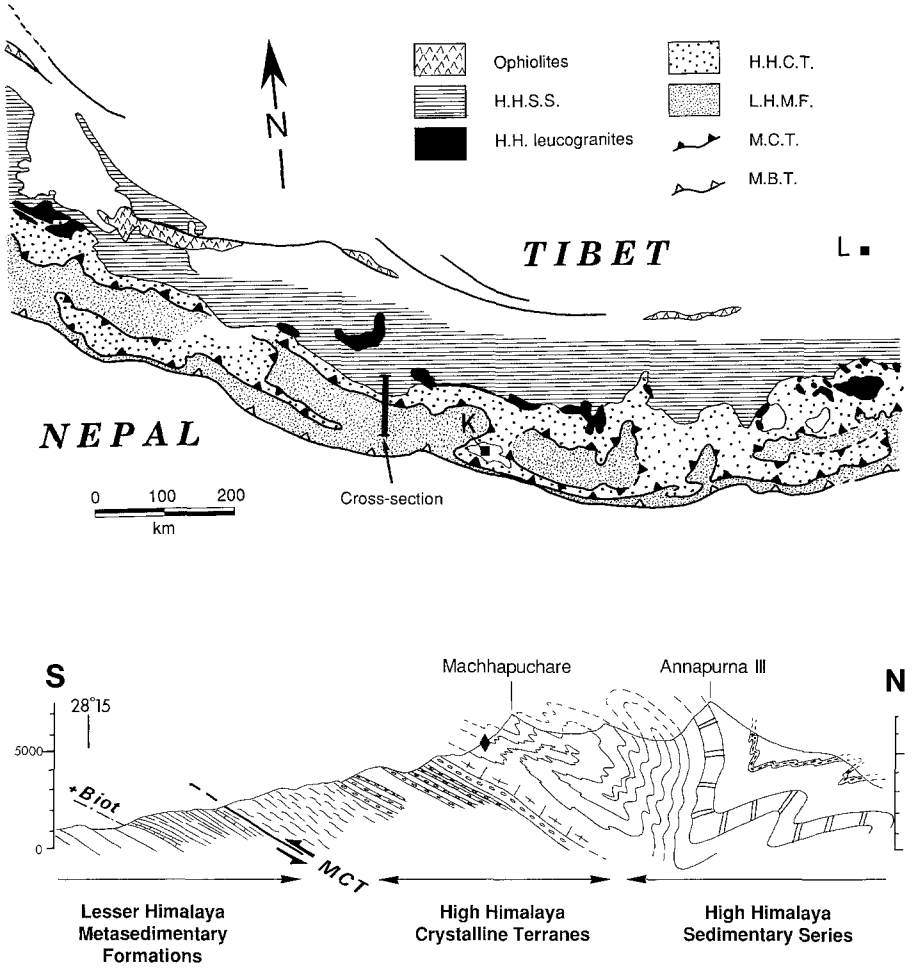

Fig. 2. Schematic map of the Himalaya between Kumaon on the West and Bhutan on the East (after France-Lanord 1987). *H.H.S.S.:* High Himalaya Sedimentary Series; *H.H.C.T.:* High Himalaya Crystalline Terranes; *L.H.M.F.:* Lesser Himalaya Metasedimentary Formations; *M.C.T.:* Main Central Thrust; *M.B.T.:* Main Boundary Thrust. Cross-section of the Annapurna Range, Nepal Himalaya after Le Fort (1975) and France-Lanord (1987). *Diamond:* situation of the NL452 sample

ing within the Indian plate (e.g. Le Fort 1975; Molnar 1984). The Main Central Thrust or MCT (Fig. 2) brought the high-grade High Himalaya Crystalline terrains (HHC or Tibetan Slab) and the High Himalaya Sedimentary Series (HHSS), onto the low-grade metasedimentary Lesser Himalaya formations.

$P-T-t$ paths calculated from mineralogical assemblages in the High Himalaya Crystalline Terrains above the MCT (Brunel and Kiénast 1986; Hodges and Silverberg 1988; Hodges et al. 1988; Pêcher and Le Fort 1986; Pêcher 1989; Hubbard 1989) indicate a clockwise path due to crustal thickening, followed by uplift and tectonic denudation. Overall in the Himalaya, this tectonic denudation results from back-sliding and back-folding in the High Himalaya Sedimentary Series (Le Fort 1975; Pêcher 1978; Bordet et al. 1981; Caby et al. 1983; Pêcher and Scaillet 1989) (Fig. 2) and normal faulting affecting some of the High Himalaya leucogranites (Burg et al. 1984; Herren 1987). In Central Nepal, the northward collapse of the HHSS could be related to a steepening or ramp of the MCT (Pêcher et al. in prep.). The major structure related to this process is the Annapurna northward recumbent anticline which is cut by the Manaslu pluton (Le Fort 1981, Figs. 1 and 6). Hence this structure is earlier than the emplacement of the 25 to 18 Ma old Manaslu granite (Deniel et al. 1987).

The sample selected for detailed examination comes from the approximately 2000 m thick Annapurna Formation of the HHSS (Fig. 2). This Cambro-Ordovician formation is dominantly composed of limestones alternating with minor schists and quartzites with a few units of felsic volcanic tuffs toward the top (Colchen et al. 1986). It shows two metamorphic schistosities. The oldest one (S1) is related to the southward thrusting of the MCT. The youngest one (S2) corresponds to northward verging large scale overturned folds (Fig. 2, Colchen et al. 1986).

The sample (NL452) was taken at 4300 m on the right lateral moraine of the Machhapuchhare glacier and comes from a 30 to 40 m^3 large moraine boulder which had detached from the inaccessible cliff of the Machhapuchare summit (6993 m). It is a S2-concordant quartz lens in the Annapurna limestones boudinaged parallel and perpendicular to the F2 fold axis. Examination of the cliff and of the map shows that S2 schistosity of the Annapurna limestones has a shallow dip toward the NNE (Colchen et al. 1986; Le Fort 1989). Therefore, the S2 schistosity plane of the sample allows us to replace it in the regional context.

The host rock of the quartz lens studied in detail is an impure limestone which contains calcite (70%), muscovite (10%), K-feldspar (15%) and accessory minerals (5%) such as rutile, oxidized pyrrhotite, graphite and minor pyrite. The texture is granoblastic and the average grain size is around 0.5 mm.

Only limited data are available on the metamorphism of the High Himalaya Sedimentary Series. There is no metamorphic hiatus between the high grade gneisses of the High Himalaya Crystalline terrains and the overlying sediments, but the metamorphic P and T conditions as observed today decrease very rapidly upwards from sillimanite gneisses (HHC) to chorite + biotite ± garnet Cambro-Ordovician metasediments (Pêcher 1989).

Analytical procedures

Fluid inclusions have been investigated in sixteen quartz lenses sampled along the Annapurna section. Three of the structurally highest samples show annular fluid inclusions. The sample studied in detail (NL452) was selected among all those samples because

it contains clearly contrasted inclusion types and exceptionally well preserved critical textural relationships.

Fluid inclusions were optically studied in thick (0.150 mm) doubly-polished sections. Microscopic observations, 2D- and 3D-orientations of the fluid inclusion planes, microthermometric measurements and Raman microprobe analyses have been done on the same 3 cm^2 section perpendicular to S2.

The 2D-orientations of the planes were measured with an interactive image analyser to obtain a quick discrimination of the fluid inclusion planes (Lapique et al. 1988; Champenois 1989). The traces of the planes are drawn and digitized on a video image. The 3D-orientation of these planes were also measured on a thick (0.5 mm) section with the focus mechanism of a petrographic microscope.

Microthermometric measurements were performed on a Chaix-Meca heating and freezing stage (Poty et al. 1976) which was calibrated at low to moderate temperature by measuring the triple point of CO_2 in a Camperio CO_2-H_2O fluid inclusion ($-56.6°$ C), of pure water (0° C) in a synthetic fluid inclusion (Zhang 1988) and of Merck compounds (CCl_4 at $-22.9°$ C, $Fe(NO_3)_3 \cdot 9H_2O$ at 47.2° C). The accuracy of the measurements is estimated at $\pm 0.1°$ C. However, the accuracy on clathrate melting temperature is $\pm 0.2°$ C because this phase change is determined from a cyclic heating/cooling procedure with a 0.2° C increment.

The analysis of the non-aqueous part of the fluid inclusions was performed at a temperature slightly higher than $ThCO_2$ with a multichannel Raman microprobe (X-Y type from DILOR company) at CREGU. The mole fraction of each gas and bulk compositions were calculated following the procedure of Dubessy et al. (1989).

Classical methods were used for quantitative extraction of structural water (Friedman 1953), of oxygen from silicates (Clayton and Mayeda 1963), and of CO_2 from calcite (McCrea 1950). Inclusion fluids were released by crushing in a stainless steel tube under vacuum. Extraction yields were manometrically measured on H_2 and CO_2 gases. Isotopic ratios were measured on H_2 and CO_2 gases using a VG 602D mass spectrometer. For NBS-28, $\delta^{18}O = 9.60‰$.

Analytical results

Texture of quartz

Quartz grains within the lens are coarse (more than 1 cm), granoblastic and almost undeformed (no undulatory extinction, a few sharp prismatic subgrain boundaries). The smooth grain boundaries contain fluid inclusions and are similar to those described by Urai (1983) in experimentally deformed wet rock salt. Fluid inclusions in grain boundaries have not been studied in detail. Most of the quartz c-axes are oriented in the S2 plane and indicate that glide on a prismatic plane was operative (Tullis et al. 1973).

Description of the fluid inclusion planes

Most of the fluid inclusions are organized in planes which represent healed fluid-filled microcracks (Smith and Evans 1984). The size of the fluid inclusions in a single plane is generally homogeneous except toward the tip of the crack where it decreases progressively. The longest fluid inclusion planes crosscut grain boundaries (intergranular cracks, Krantz 1983), but many of them are shorter than the grain size and are therefore intragranular (Krantz 1983). The length of fluid inclusion plane discriminates the different types of fluid inclusion populations. This length is a minimum estimation as it is measured on a thick section. Finally, the filling ratio of the fluid inclusions within a single plane is constant if the fluid inclusions were not reworked by decrepitation or intersection with another plane.

Table 1. Characteristics of the different types of fluid inclusions

Type	Shape	Size[a] μm	Orientation of planes	Length of planes	Nature % CO_2	Tm CO_2 ±0.1° C	Tm clath ±0.2° C	Th CO_2 range	ΔTh CO_2 in a plane
1	ellipsoidal smooth walls	<20	isolated no planes		CO_2+H_2O 90–95	−56.7		−19 to −11 L	
2	annular	10 to 150	high angle to S2	up to 15 mm	CO_2+H_2O 90–95	−56.7		−2.4 to +8.3 L	up to 8
3	regular, spherical or ellipsoidal	< 6	high angle to S2	<25 mm	CO_2+H_2O 90–95	−56.7	+9.1 to 9.6	5 to 29.5 L	<2
4	irregular	<12	oblique to S2	< 2 mm	CO_2+H_2O >95	−56.7	+9.1 to 9.6	+25 to 30.9 L 30.9 to 16.2 V 31.1 C	<2
5	annular or irregular black	50 to 150	high angle to S2	up to 15 mm	n.d.			+30.2 V (1 measure-ment)	
6	irregular	< 5			H_2O or H_2O+CO_2	−56.7	Tm ice = −0.4 H_2O −3.8 H_2O+CO_2		

[a] Longest dimension, Tm: temperature of melting, Th: temperature of homogeneisation
%CO_2: volume percent of the CO_2-rich phases at room temperature. n.d.: non determined
L, V, C: homogeneisation into the liquid, vapour or critical phase

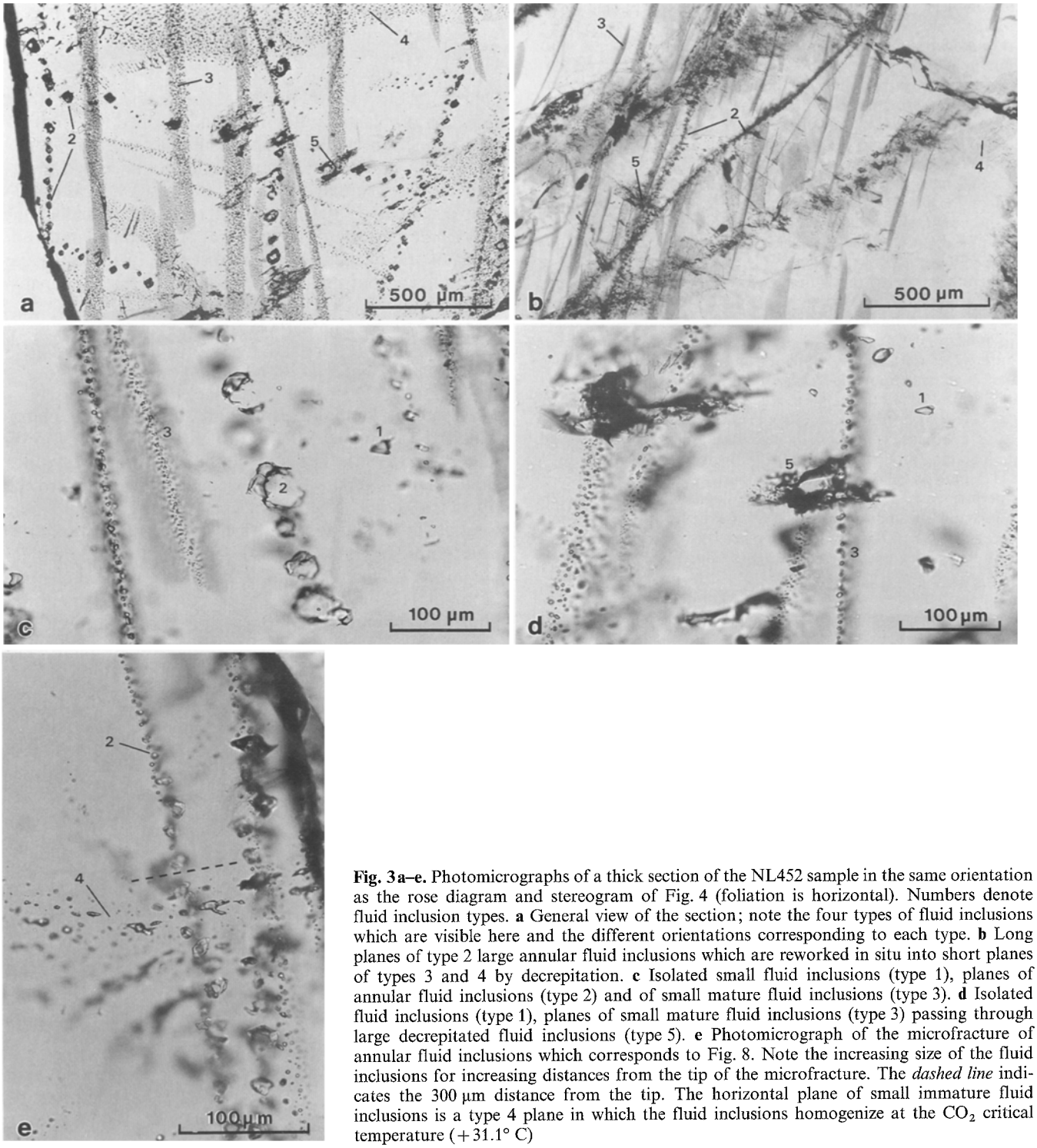

Fig. 3a–e. Photomicrographs of a thick section of the NL452 sample in the same orientation as the rose diagram and stereogram of Fig. 4 (foliation is horizontal). Numbers denote fluid inclusion types. **a** General view of the section; note the four types of fluid inclusions which are visible here and the different orientations corresponding to each type. **b** Long planes of type 2 large annular fluid inclusions which are reworked in situ into short planes of types 3 and 4 by decrepitation. **c** Isolated small fluid inclusions (type 1), planes of annular fluid inclusions (type 2) and of small mature fluid inclusions (type 3). **d** Isolated fluid inclusions (type 1), planes of small mature fluid inclusions (type 3) passing through large decrepitated fluid inclusions (type 5). **e** Photomicrograph of the microfracture of annular fluid inclusions which corresponds to Fig. 8. Note the increasing size of the fluid inclusions for increasing distances from the tip of the microfracture. The *dashed line* indicates the 300 µm distance from the tip. The horizontal plane of small immature fluid inclusions is a type 4 plane in which the fluid inclusions homogenize at the CO_2 critical temperature (+31.1° C)

Types of fluid inclusions

Six types were identified according to the geometry of fluid inclusions and planes and of the microthermometric data (Table 1). The timing from oldest to youngest type was established on the basis of classical geometric criteria (see Touret 1981; Roedder 1984). Most of the fluid inclusions contain CO_2-H_2O fluids. Their filling ratios, estimated optically, are very imprecise especially for high CO_2 contents. In some very regular fluid inclusions, only a clathrate formation indicates the presence of water. As shown in Table 1, the melting temperatures of CO_2 in the presence of vapour and liquid phases are suprisingly constant for all types of fluid inclusions

($-56.7 \pm 1°$ C). Also the dissolution temperatures of clathrate are very constant whatever the fluid phase assemblage (9.1 to $9.6 \pm 0.2°$ C).

Type 1. Isolated fluid inclusions. They are small to medium size (< 20 μm, Fig. 3c), isolated or in small groups of less than ten inclusions. They represent less than 1% of the total number of fluid inclusions in the sample and are observed only near type 2 healed microcracks at a distance less than 125 μm. They contain CO_2 and H_2O. At room temperature the carbonic phase (90–95 vol.%) is a liquid; hence $ThCO_2$ to the liquid phase is below room temperature. They provide the lowest value for $ThCO_2$ of the sample ($-19.0°$ C) and show an asymmetric distribution of $ThCO_2$ toward low temperatures (Fig. 6). Most values are in the -5 to $+5°$ C range. The dispersion is important even for inclusions of a single group. Their chronology relative to the other types is not clearly established.

Type 2. Annular fluid inclusions. They are medium size to large (10 to 150 μm, Fig. 5), CO_2-H_2O bearing and have an annular shape (Fig. 3a, b, c and e). They are organized in healed transgranular microcracks up to 15 mm long (Fig. 5). The size of the inclusions decreases towards the tip of the microcrack and the smallest ones (< 10 μm) do not show any annular shape (Fig. 3e).

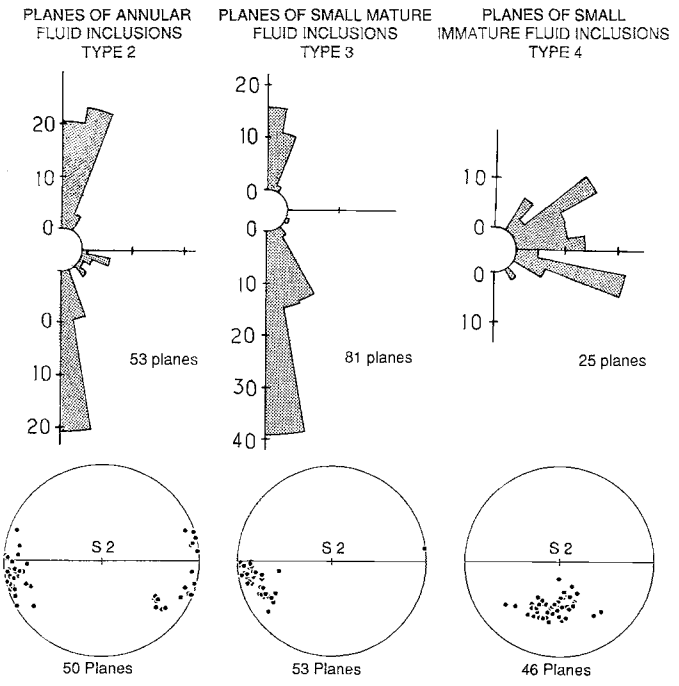

Fig. 4. Rose diagrams showing the percentage in length of fluid inclusion planes as a function of the direction measured in a plane perpendicular to the S2 schistosity (horizontal reference line). Stereographic projections (lower hemisphere) of the fluid inclusion planes

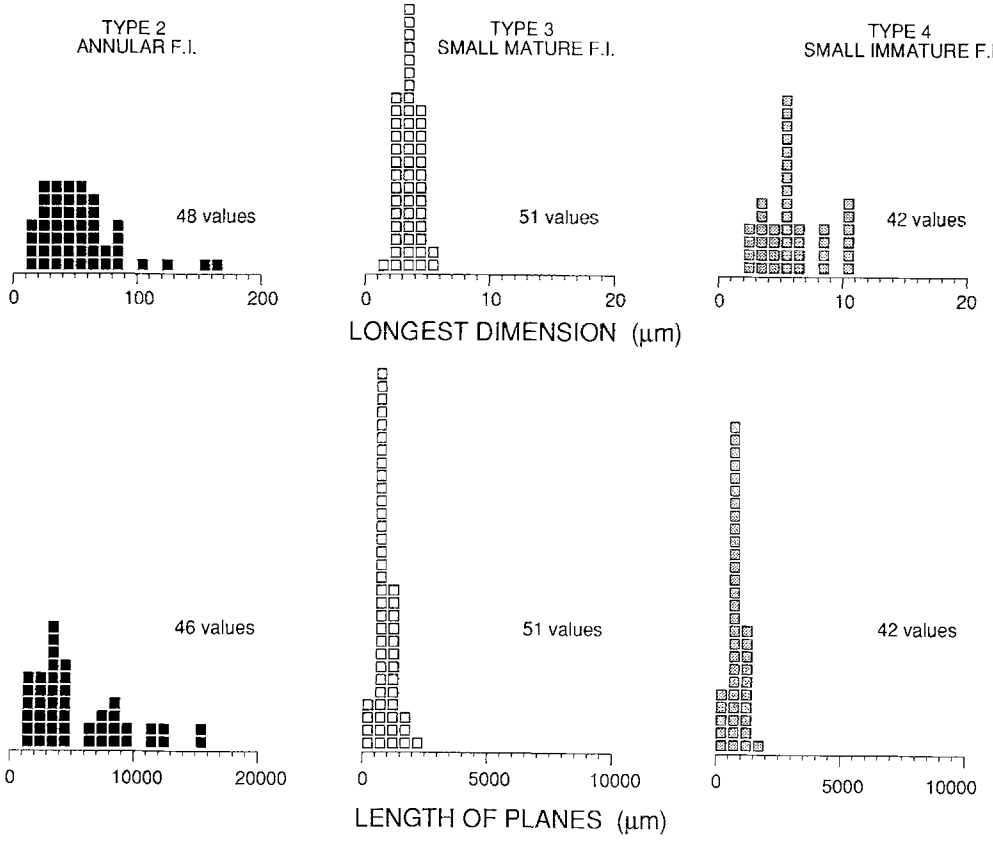

Fig. 5. Histograms of the longest dimension of fluid inclusions as measured in thick section, and of the length of the fluid inclusion planes. Note the different ranges for type 2 and types 3 and 4 fluid inclusions

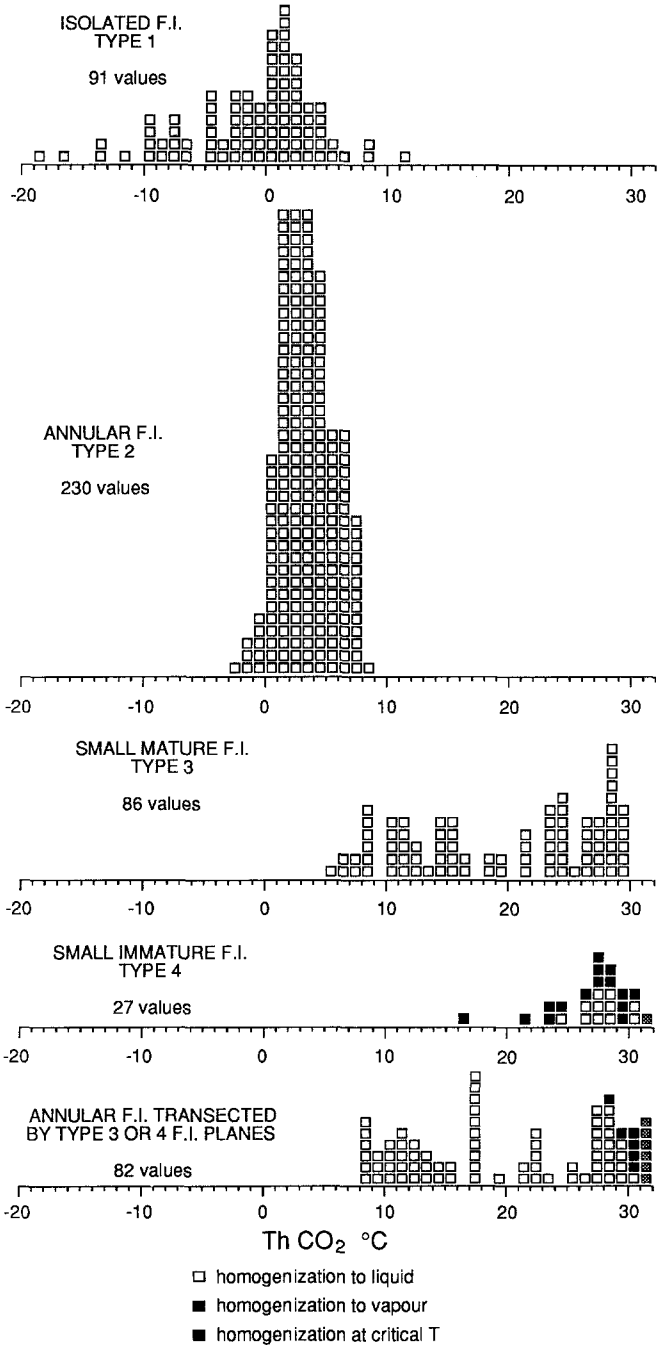

Fig. 6. Histograms of $ThCO_2$ values for the different types of fluid inclusions. One *square* represents one measurement except for the type 3 and 4 planes for which the median value of each plane is reported

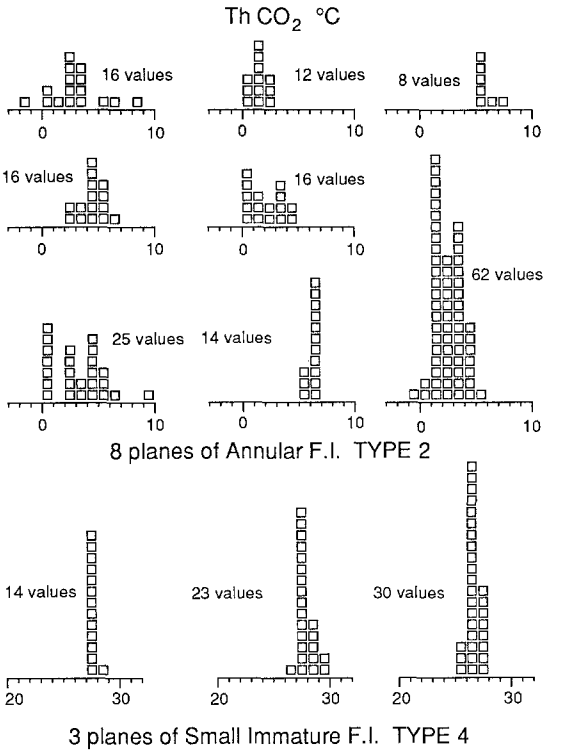

Fig. 7. Histograms of $ThCO_2$ values for annular (type 2) or small immature (type 4) fluid inclusions in a single plane. One *square* represents one measurement. Note the dispersion of a few degrees for the annular fluid inclusions and the absence of dispersion for the small immature fluid inclusions

Therefore the ≈10 μm dimension appears to be a minimum diameter for annular fluid inclusions. They are commonly surrounded by a few smaller inclusions and the rings are locally stretched into two or three smaller inclusions. The planes are organized following one major orientation perpendicular to S2 and one minor orientation at a low angle to S2 (Fig. 4).

The shape of fluid inclusions changes with the orientation of host quartz c-axis relative to the S2 schistosity. Frequently, the *c* axis is at a low angle to S2, large fluid inclusions are annular, and the ring contains the *c* axis. By contrast, in crystals with *c* axis nearly perpendicular to S2, fluid inclusions display a negative crystal shape made of two pyramids. Therefore, the development of the annular shape is crystallographically controlled.

Annular fluid inclusions contain 90–95% volume of CO_2. At room temperature, the carbonic phase is a liquid except where the type 2 inclusion plane is intersected by a plane of type 3 or 4 inclusions (Fig. 3a, c and e).

$ThCO_2$ (to the liquid phase) values range from −2.4° C and +8.3° C (Fig. 6). In a single microfracture the dispersion remains high, up to 8° C (Fig. 7). Measurements, on a single microcrack, of $ThCO_2$, inclusion diameter and distance from the tip of the crack are given in Fig. 8. The fluid inclusion (F.I.) diameter increases and the $ThCO_2$ decreases in the first 300 μm of the crack. Therefore inverse correlation exists between the F.I. diameter and the $ThCO_2$. At longer distances no correlation exists any more. The largest variation of $ThCO_2$, between the fluid inclusion of the tip of the crack and the lowest $ThCO_2$ in the crack, is 5° C.

Higher $ThCO_2$ (+8.8 to +30.2° C in the liquid phase; +31.1° C in the critical phase; and +31.0 to +28.3° C in the vapour phase) occur at the intersection with type 3 or 4 planes. These values correspond to those measured from the cross-cutting type 3 or 4 microcracks (Fig. 6). This relationship shows that type 2 inclusions

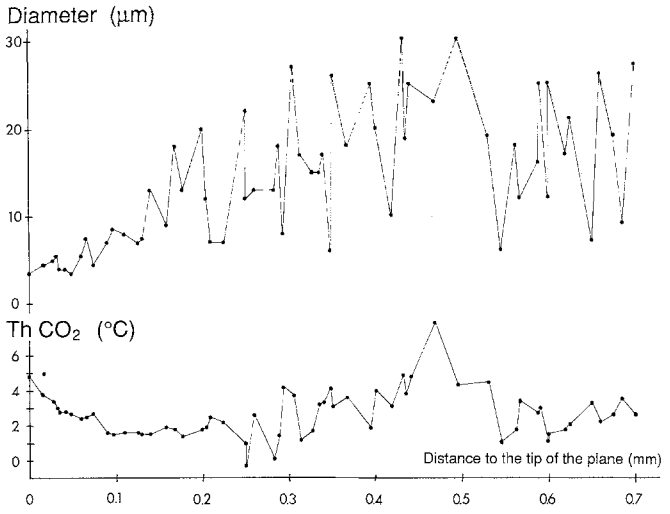

Fig. 8. Diagrams showing the CO_2 homogenization temperature and the diameter of the annular fluid inclusions versus the distance from the tip of the fluid inclusion plane. Note the decreasing $ThCO_2$ for the increasing diameter of fluid inclusions near the tip of the microfracture. These measurements have been performed on the type 2 microfracture of Fig. 3e

Table 2. Raman microprobe analyses on types 2, 3, 4 fluid inclusions

Type of F.I.	$ThCO_2$ °C	CO_2 mol%	CH_4 mol%	N_2 mol%	H_2S mol%
2	+ 1.0	98.6	0.05	1.2	0.15
3	+15.0	98.7	0.07	1.1	0.16
4	+27.5	97.8	0.15	1.9	0.15

are earlier than types 3 and 4. Such intersection relationships were also described by Pagel (1975).

One typical annular fluid inclusion was selected for Raman microprobe analysis on the basis of its $ThCO_2$ (+1.0° C to the liquid phase) close to the mean value. The volatile component of this inclusion shows a very high molar proportion of CO_2 (98.6%) and some traces of other gases (CH_4, N_2 and H_2S, see Table 2).

Type 3. Small mature fluid inclusions. They are small (<6 μm, Fig. 5) CO_2-H_2O fluid inclusions (Fig. 3a to d), with a regular or mature shape (spherical or ellipsoidal). They define one direction of planes (Fig. 4) parallel to the main orientation of type 2. Type 3 fluid inclusion planes are generally short (less than 2.5 mm; Fig. 5). A large decrepitated fluid inclusion is generally present at the center of the planes (Fig. 3b). The filling ratio is constant in a single plane at approximately 90 to 95 vol.% of CO_2. The carbonic phase is either single or two-phase at room temperature. Increased size of the CO_2 vapour bubble at the intersection of types 3 and 4 planes, shows that type 3 planes are earlier than type 4 ones.

Minimum and maximum $ThCO_2$ were measured for every healed microfracture and only their mean value is reported on the histogram (Fig. 6) because of the large number of inclusions in a single plane and of the narrow range of homogenization temperature (less than 2° C). Homogenization of CO_2 always occurred to the liquid phase between +5.0° C to +29.5° C.

One type 3 fluid inclusion with $ThCO_2$ close to the mean value ($ThCO_2$ = 15.0° C to the liquid phase) was analysed with the Raman microprobe (Table 2). Its volatile component is very similar to the analysed type 2 inclusion: 98.7 mol% of CO_2 and traces of CH_4, N_2 and H_2S.

Type 4. Small "immature" fluid inclusions. They are small (<12 μm, Fig. 5) CO_2-H_2O bearing and irregular in shape. Type 4 fluid inclusion planes are short, intragranular and are at low angle to S2 (Fig. 4). They are commonly localized around large decrepitated type 2. The CO_2 volume percent is approximately 95 vol.% or more. The carbonic part is two-phase, with a large vapour bubble and a liquid, at room temperature (Fig. 3e).

$ThCO_2$ are quite constant within a single plane (Fig. 7). Mean values of $ThCO_2$, calculated for each fluid inclusion plane as for type 3, vary between +16 and +31° C (Fig. 6). Homogenization of CO_2 occurs either to the liquid, between +25° and +30.9° C, or to the vapour phase, between +16.2 and +30.9° C. One fluid inclusion plane has been observed with a critical homogenization of CO_2 at +31.1° C for each inclusion.

The type 4 fluid inclusion selected for Raman analysis ($ThCO_2$ = +27.5° C to the liquid phase) shows a high molar proportion of CO_2 (97.8%) and traces of CH_4, N_2 and H_2S (Table 2). Therefore, it is very similar to types 2 and 3 fluid inclusions.

Type 5. Large dark fluid inclusions. They are medium to large size (50 to 150 μm) dark inclusions (Fig. 3a and d). They belong to type 2 planes and are surrounded by numerous small fluid inclusions or transected by type 3 or 4 microcracks. An aqueous and a vapour-rich carbonic phase can occasionally be identified. These inclusions are frequently transected by short fractures parallel to a prismatic plane. They are interpreted as decrepitated type 2 inclusions, from their size and position. Microthermometric measurements were not possible on these dark fluid inclusions.

Type 6. Small water-rich fluid inclusions. They are rare and small (<5 μm) H_2O or H_2O-CO_2 rich fluid inclusions. They are locally observed in the vicinity of type 5 or related to rare and short microcracks.

The water rich fluid inclusions associated with the large dark type 5 show melting temperature of ice around −3.8° C where CO_2 is present, and −0.4° C in pure H_2O fluid inclusions, both indicating very low salinity. $ThCO_2$ in the former is high (one measurement at +30° C to the vapour phase). Bulk homogenization temperatures for purely aqueous inclusions are greater than 90° C; they were not measured however, in order to prevent decrepitation of carbonic inclusions.

Stable isotopes

Isotopic data are given in Table 3. The CO_2/H_2O molar ratio of the released gases is 6.1 and is consistent with the filling ratio observed under the microscope (90–95 vol.% for all types except type 6). However, because fluids were released by crushing, this ratio reflects a mixing of all fluid inclusion populations. It can be roughly estimated that type 2 and 3 fluid inclusions are in equivalent proportions and together represent 85 to 95% of the whole. Therefore the isotopic data can be interpreted as primarily representing types 2 and 3 fluids.

Table 3. H, O and C isotope data on sample NL 452

Phase		δD ‰ smow	$\delta^{18}O$ ‰ smow ±0.2	$\delta^{13}C$ ‰ PDB ±0.2
Fluid inclusions (sample weight: 13.2 g; extracted: 10.6 μmolH_2O, 67.6 μmolCO_2)				
H_2O	14 mol%	−92.0±5		
CO_2	86 mol%			+1.9
Muscovite	4.6 wt% H_2O^+	−53.5±2	+19.4	
Quartz			+21.9	
Calcite			+20.6	−1.3

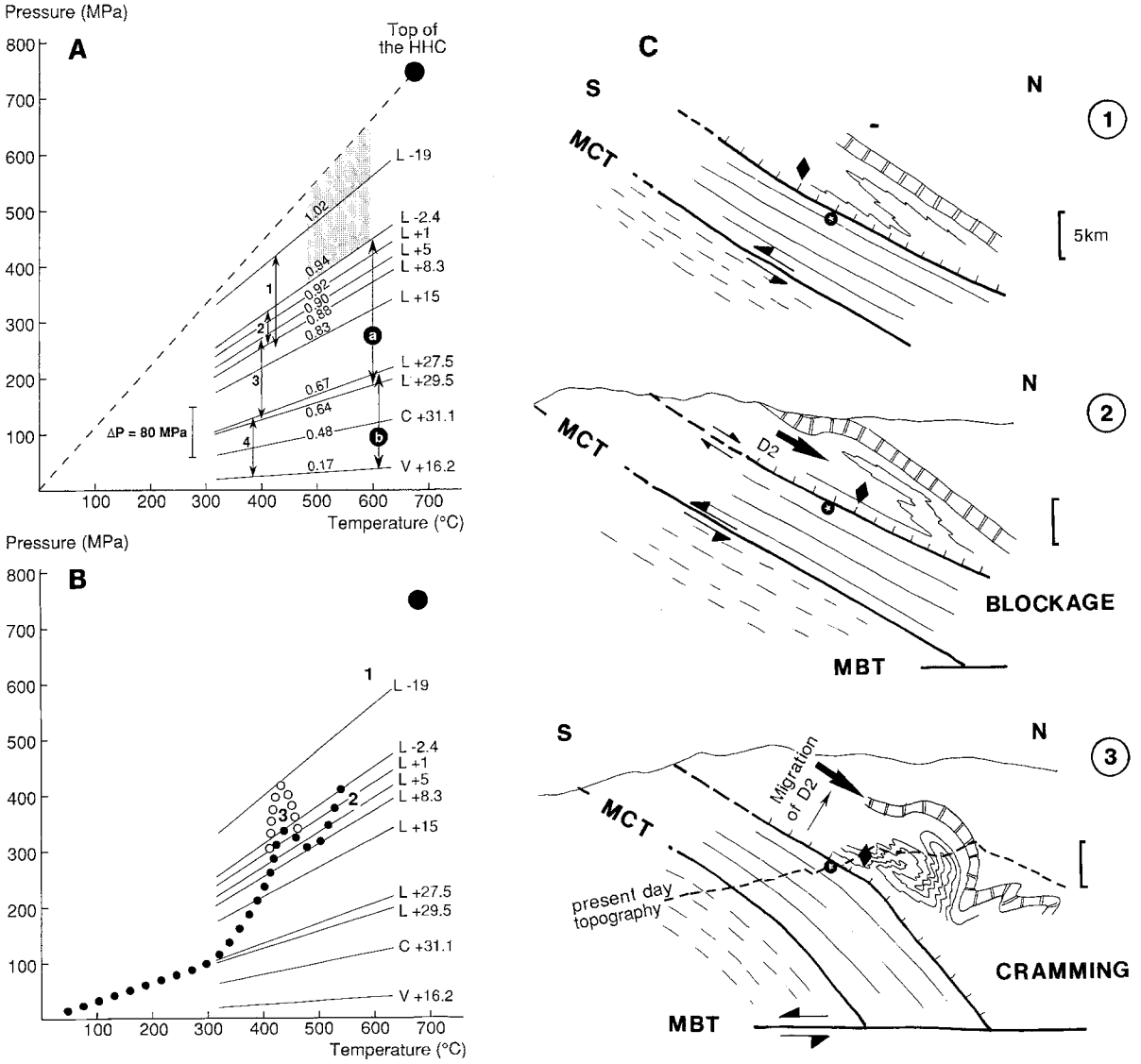

Fig. 9. A Pressure – temperature diagram showing the calculated isochores for different types of fluid inclusions. The $ThCO_2$ (° C) (L = to the liquid, C = to the critical, V = to the vapour phase) and the density (in g/cm^3) corresponding to each isochore are reported in the diagram. The numbers refer to the different types of fluid inclusions. a and b correspond respectively to the first (types 2 and 3) and to the second (type 4) orientations of healed microcracks. The (*P*, *T*) conditions estimated from mineralogical assemblages in a sample on the top of the High Himalaya Crystalline Terranes (Tibetan Slab, Annapurna section, Le Fort et al. 1986) are also reported on this diagram (*black circle*). The *dashed area* indicates the temperature range for the D2 deformation. ΔP = 80 MPa is the quartz strength and the value of internal overpressure above which a large fluid inclusion decrepitates (Leroy 1979; Sterner et al. 1989). **B** Interpreted (*P*, *T*, *t*) paths of the NL452 sample. Two values of pressure increase are proposed depending on the interpretation of buffered 1 fluid inclusion (see discussion in text). **C** Cartoon showing the structural history of the High Himalayan pile (see explanations in text)

Hydrogen. δD values of fluid inclusion water and of muscovite are -92‰ and -53.5‰ respectively. According to the experiments of Suzuoki and Epstein (1976) muscovite should always be depleted in D relative to coexisting H_2O fluid at temperatures lower than 750° C. Therefore muscovite cannot be in isotopic equilibrium with the fluid inclusion water.

Oxygen. The $\delta^{18}O$ values of coexisting quartz, calcite and muscovite are respectively 21.9, 20.6 and 19.4‰ (Table 3). Such high values reflect the limestone environment which probably buffers oxygen isotopic compositions. Isotopic temperature calculated from isotopic fractionations ($\Delta_{Q-Cc}=1.3\pm0.4$ and $\Delta_{Q-Mu}=2.5\pm0.4$) are 575° C$\pm$70 for quartz-muscovite (Bottinga and Javoy 1973) and 410° C$\pm$100 for quartz-calcite (Clayton et al. 1972, combined with O'Neil et al. 1969). The large difference between calculated temperatures is due to (1) possible small disequilibrium and (2) the inaccuracy of these geothermometers. Nevertheless these fractionations are consistent with equilibrium at temperatures around 400–500° C.

Carbon. $\delta^{13}C$ value is 1.9‰ for CO_2 from fluid inclusions and -1.3‰ for calcite of the host rock. These values are typical of carbonated environments. CO_2-calcite carbon isotope fractionation is 3.2 ± 0.4 which is a little higher than the maximum fractionation (2.8 at 450° C, Bottinga 1968).

Bulk $V-X$ properties and representative isochores

Bulk molar compositions have been calculated for the three fluid inclusions analysed by Raman microprobe (types 2, 3 and 4). This calculation is based on the methodology developed by Ramboz et al. (1985) and Dubessy et al. (1989). The salinity was assumed to be zero in CO_2-rich inclusions. A step by step calculation from 2 to 20 vol.% of H_2O was performed because the CO_2/H_2O filling ratio is not precisely known. This step by step calculation was applied also to fluid inclusions showing the extreme values of $ThCO_2$ in types 1 to 4. The volatile part was assumed to be identical for all fluid inclusions of the same type. The volatile part in type 1 was considered to be similar in composition to type 2 on the basis of microthermometric data. This step by step calculation indicates that a variation of 2 to 20 vol.% of H_2O induces only a slight variation in bulk density but an important variation of the bulk composition. Consequently, and as all types of fluid inclusions show almost identical filling ratios (90 to 95 vol.% CO_2), the bulk composition and density chosen for further isochore calculation is the value measured by crushing for isotopic study (CO_2/H_2O molar ratio$=6.1$). This choice is justified below on the basis of textural evidence.

Isochores were calculated using the equation of state of Kerrick and Jacobs (1981) for fluid inclusions displaying the mean and extreme values of $ThCO_2$ in each type. These isochores show that $P-T$ overlaps exist between all types of fluid inclusions (Fig. 9).

Discussion

Quartz texture and D2 phase

The macroscopic boudinage of the lens, the large size of the quartz grains, the smooth grain boundaries and the lack of deformation microstructure indicate that the quartz was plastically deformed but subsequently recrystallized by grain boundary migration during the D2 event. This grain boundary migration was probably enhanced by the presence of a fluid phase in the grain boundaries (Urai 1983). The preferred orientation of quartz *c*-axes suggests gliding on prismatic planes (Tullis et al. 1973). In quartz, prismatic glide and grain boundary migration occur at temperatures of 450° C and above (Tullis et al. 1973; Bouchez and Pêcher 1981). This value is consistent with temperature calculated from C and O isotope fractionations. As fluid inclusion planes described in the NL542 sample cut across grain boundaries (types 2 to 4), they should postdate the D2 deformation event.

Evolution of the stress field

The orientation of the fluid inclusion planes is not crystallographically dependent, but can be correlated with the regional stress field as shown by Tuttle (1949), Lespinasse and Pêcher (1986) and Laubach (1989). Fluid inclusion planes are considered here to be healed extensional fluid-filled microcracks, that is, microcracks contained in the (σ_1, σ_2) plane and opened in the σ_3 direction (see Krantz 1983), as are most of the observed microcracks in rocks. Consequently, two successive orientations of the stress field may be deduced from the fluid inclusion planes in sample NL452 (Fig. 4). The first one is represented by type 2 and 3 fluid inclusions and corresponds to a (σ_1, σ_2) plane nearly perpendicular to the S2 foliation. The second one is represented by type 4 fluid inclusions and corresponds to a stress field in which the (σ_1, σ_2) plane is at low angle to S2. The 3D-orientation of fluid inclusion planes (stereographic projections, Fig. 4) shows no gap between distributions of types 3 and 4. Therefore, as type 3 is older than type 4, $\sigma 3$ direction progressively shifted in an oblique plane relative to the S2 schistosity. These two stress fields postdate the plastic deformation event. The absence of rotation of the D2 fold axis and of deformation of the quartz suggests that a passive rotation of the sample relative to the regional coordinates is highly improbable. Therefore, these two stress fields are interpreted as representative of a rotation of the regional (σ_1, σ_2) plane.

Chronology of fluid inclusion types

Two explanations may be suggested for the origin of type 1 fluid inclusions. First, they can be fluids left behind migrating grain boundaries (see Urai 1983) and would be earlier than the other types. Second, they can probably represent fluid inclusions stretched from type

2 planes as shown by their close spatial association with type 2 planes. Dispersion of fluid inclusions away from their plane is often described (see discussion in Roedder 1984, pp 66–68). However, both interpretations will be considered in the next discussion as we have no absolute evidence for the origin of type 1. On the basis of textural and microthermometric data, it has been demonstrated that the chronology of the other types is the following: 2, 3, 4, 5 and then 6.

Density evolution

The evolution of bulk density is discussed in terms of density of the carbonic component or in terms of $ThCO_2$ because the water content remains approximately constant in all types of fluid inclusions.

Types 1 and 2. The $ThCO_2$ distribution in the tip of a single type 2 fluid inclusion plane strongly suggests that the density of the fluid increased after healing of the crack. The larger the fluid inclusion, the greater is the increase in density. This correlation between size and density of the fluid inclusion remains true as long as there is no necking of a previous inclusion into several smaller inclusions. At a distance greater than 300 μm from the tip, this correlation is not valid any more because necking is common (see distribution of diameter on Fig. 8). A minimum density increase may be estimated from the difference in $ThCO_2$ in the single microcrack ($\Delta T = 5°$ C, that is $\Delta d = 0.03$ g/cm^3). These observations are consistent with results of burial-simulating experiments where internal pressure in the fluid inclusion was lower than the confirning pressure and induced a volume-dependent increase of density.

The annularization of type 2 fluid inclusions is interpreted as occurring during this change in density. Comparison with experiments by Pêcher (1981) also leads to the interpretation that the annular fluid inclusions are induced by external overpressure ($\Delta P > 0$) in an anisotropic stress field. The crystallographic control of annular fluid inclusions remains to be quantified with respect to the stress field.

The duration of external overpressure probably was short because the annular shape is not an equilibrium shape. An increase of confining pressure would have been the more efficient process to produce a short-lived external overpressure. The annular fluid inclusions and the observed density increases are interpreted as a consequence of a short-lived burial or loading of the High Himalaya Sedimentary Series.

In the previous section, two interpretations have been presented for the origin of type 1 fluid inclusions. Following the first one, these inclusions represent earlier intergranular fluids trapped during syn-D2 recrystallization and therefore, indicate the $P-T$ conditions of this tectonic event. As temperature is estimated at 400–500° C from textures and isotope fractionations, a pressure range of 300–400 MPa may be deduced from the mean value of $ThCO_2$. Scattering of $ThCO_2$ toward lower temperatures may indicate that D2 deformation has preserved older fluid inclusions or that the recrystallization process began at higher pressure. If this first interpretation for type 1 is chosen, then the increase of confining pressure subsequent to the emplacement of type 2 microcracks is deduced from the increase in density in a single type 2 microcrack, that is 30 to 40 MPa at 400 to 500° C (black dots on Fig. 9B). The second interpretation, based on the dispersion of type 2 inclusions away from the healed microcrack would explain the similar peaks of $ThCO_2$ for types 1 and 2, as well as the asymmetric scattering of $ThCO_2$ toward lower temperatures for type 1 fluid inclusions (Fig. 6). Following this interpretation of type 1, the maximum density increase induced by external overpressure might be as large as 0.10 g/cm^3, calculated from the maximum density of type 1 or 2 fluid inclusions (1.02 g/cm^3 i.e. $ThCO_2 = -19.0°$ C). This density increase would correspond to a confining pressure increase of 125 MPa at 600° C, or 100 MPa at 350° C (open dots on Fig. 9B).

Types 3 and 4. The narrow range of $ThCO_2$ values in a single plane (less than 2° C) for type 3 and 4 fluid inclusions suggests that they remained unchanged after trapping. Therefore, the scattering of densities deduced from $ThCO_2$ values for different cracks of types 3 and 4, is interpreted as due to trapping of a fluid at decreasing pressures and temperatures.

The immature shape of type 4 inclusions indicates poorly healed microcracks and is consistent with lower trapping temperature compared to the mature type 3 (Smith and Evans 1984).

Types 5 and 6. The decrepitated type 2 fluid inclusions (type 5) and spatially associated water-rich (type 6) inclusions may be attributed to the continuation of the pressure-temperature drop registered by type 3 and 4 inclusions.

Such a drop in P and T conditions should also have modified the shape and density of type 1 and 2 fluid inclusions. However, these changes cannot be evidenced, first because the density decrease related to this stage should have been volume independent and therefore identical for all fluid inclusions whatever their size. Second, as temperature decreases; it precludes significant plastic deformation of quartz around fluid inclusions and consequently, large volume change of these inclusions. Thus, this P and T drop is considered to have had negligible effects on types 1 and 2 inclusions except to decrepitate the largest ones.

To summarize, fluid inclusions of sample NL452 indicate a complex multi-stage density evolution. If we retain the interpretation of dispersion of type 2 for type 1, the first stage is represented by type 2 fluids, with an estimated density of about 0.92 g/cm^3. The second stage corresponds to an increase of density or increase of confining pressure recorded by the annularization of type 2 (minimum pressure increase of 30 MPa, maximum pressure increase of 100 MPa at 350° C). Finally, decreasing densities (0.90 to 0.17 g/cm^3) are represented by types 3 to 6, and correspond to a drop in P and T conditions.

Chemistry and origin of fluids

The gas composition remains constant from types 2 to 4. Although it is impossible to measure accurately the water content, the filling ratio seems to be constant. This indicates that the percolating fluids were either constant in composition through time or were locally buffered by mineral assemblages of the surrounding rocks. On the basis of O and C isotope compositions, the CO_2-bearing fluid, the minerals of the quartz lens and the surrounding rock are all close to equilibrium which supports the buffering hypothesis. Moreover sulphur activity has been calculated at different temperatures from the H_2S content determined by Raman analysis following the calculation method of Dubessy et al. (1989, 1990). When plotted in a diagram of S_2 activity as a function of temperature (Toulmin and Barton 1964; Barnes 1979), the a_{S_2} falls in the stability field of pyrrhotite for temperatures above 450° C for types 1 and 2 fluid inclusions, and above 400° C and 350° C for types 3 and 4 respectively. As pyrrhotite is present in the surrounding impure limestones, the percolating fluids were always in equilibrium with the surrounding rock in a decreasing temperature path.

Another explanation for the stability of fluid chemistry is the in situ reworking of the fluids trapped in type 2 microcracks. Local reworking of type 2 fluid inclusions by decrepitation into types 3 and 4 microcracks is supported by the intragranular nature of the latter and by their localization on large decrepitated type 2 fluid inclusions (Fig. 3b). This process occurred in the single fluid phase as all cracks display the same filling ratio.

It is difficult to determine precisely the origin of the fluids from isotopic compositions of the CO_2 bearing fluid and the quartz vein because they are buffered by the surrounding rocks. CO_2 could percolate from the underlying formations as it is present in the metamorphic fluids found in the Tibetan Slab and below the MCT (Pêcher 1979; Sauniac and Touret 1983; Craw 1990). The alternative would be decarbonation reactions in the HHSS. This has been poposed by Leroy et al. (1975) who report up to 70 mol% of CO_2 in fluid inclusions of quartz crystals bearing fractures in similar formations from the northern side of the Annapurna. Typical $\delta^{13}C$ values of carbonated rocks in the HHSS are between 0 and -4‰ (France-Lanord et al. 1988, Table 3) which are compatible with decarbonated CO_2 at $+1.9$‰. In contrast to CO_2, the origin of the H_2O is certainly external, but has experienced a hydrogen isotope shift through time, as shown by the disequilibrium between muscovite and water. The δD value of muscovite (-53.5‰) is very similar to δD values of muscovite found in the underlying Tibetan Slab (-45 and -65‰: France-Lanord 1987; France-Lanord et al. 1988, Table 4). The δD value of the bulk water of fluid inclusions, -92‰, is intermediate between the metamorphic fluids of the Tibetan Slab (≈ -40 to -60‰) and fluids found in quartz veins in the Tibetan Sedimentary Series surrounding the Manaslu pluton (-120 to -130‰). For these veins a meteoric origin of water has been demonstrated (France-Lanord et al. 1988, Table 3). Therefore, two components at least can be proposed for water in the vein NL 452: (1) metamorphic water which equilibrated with muscovite and was probably present at the time of lens formation, and (2) meteoric water which percolated through the lens in microcracks, but was not pervasive as muscovite has kept its "original" D/H metamorphic composition. It is suggested that the two waters were mixed at the trapping stage in the cracks for the following reasons: (1) even if they are syn-D2 and metamorphic in origin, type 1 fluid inclusions contribute less than 1% in volume, (2) types 2 and 3 represent 85 to 95% of the whole extracted fluid and type 3 derives from type 2 by in situ decrepitation. Therefore, the isotopic compositions are considered as representative of type 2, thus resulting from mixing of the two waters before trapping.

Reconstruction of the $P-T-t-\varepsilon-\sigma$ history

The proposed $P-T$ evolution of the studied sample reconstructed from the complex multi-stage density evolution is represented in Fig. 9. Metamorphic CO_2-H_2O rich fluids percolated through the rock during and after the deformation related to southward thrusting of the whole pile (Lesser Himalaya Formation, High Himalaya Crystalline Terrains and High Himalayan Sedimentary Series). During this stage muscovite crystallized in isotopic equilibrium with a metamorphic fluid which had the same hydrogen isotopic signature as the fluids percolating through the High Himalaya Crystalline Terrains (France-Lanord et al. 1988). Quartz veins formed and their oxygen isotopic composition was buffered by the surrounding limestones. P and T conditions at the end of this stage have been estimated at around 760 MPa and 680° C by Le Fort et al. (1986) for the top of the High Himalaya Crystalline Terrains in the Annapurna section.

Afterwards, the thickening of the crust induced a tectonic denudation by collapse of the upper terrains towards the north (D2 deformation in the High Himalaya Sedimentary Series). At this stage, a high shear strain (ε) took place at the base of the Series and quartz veins were boudinaged in the S2 schistosity corresponding to extensional tectonics. This deformation probably took place at high temperature (above 450° C, 1 on Fig. 9C) on the basis of texture and isotopic oxygen fractionations. Pressure may be constrained below the line between the top of the HHC and the mean isochore for type 2 inclusions, i.e. more than 300 MPa (Fig. 9A).

After the extensional shear deformation, meteoric water percolated through the rocks, mixing with metamorphic fluids. The mixed fluids were trapped in microcracks (type 2 fluid inclusion planes, nearly perpendicular to the S2 schistosity, 2 on Fig. 9C). This stage still occurred above 450° C based on the a_{S_2} value and presence of pyrrhotite. Pressure deduced from type 2 isochores, was around 300 MPa at 450° C (Fig. 9A).

In the following stage (3 on Fig. 9C), the type 2 fluid inclusions were transformed into annular fluid inclusions and the pressure increase is estimated to be 40 MPa or

100 MPa, depending on the interpretation of type 1 fluid inclusions. This stage is supposed to have occurred at high temperature to allow plastic deformation of quartz around fluid inclusions, i.e. around 400 to 450° C. This increase in pressure was short in duration and may be correlated with loading resulting from collapse and backfolding of the levels structurally above the Annapurna limestones.

Then, type 3 fluid inclusions were generated mostly by decrepitation of large type 2 fluid inclusions and in planes again nearly perpendicular to the schistosity. This occurred during the subsequent uplift of the pile in a P and T range of 300 to 100 MPa and 400 to 300° C. Therefore, the stress orientation remained constant from the trapping of types 2 to 3 (Fig. 9B). The short-lived increase in pressure recorded by annularization represents, therefore, a minor episode during the whole uplift history of the Annapurna Range, induced by a possible ramp on the MCT (Caby et al. 1983) (Fig. 9B).

Finally the stress tensor rotated and large fluid inclusions decrepitated to generate type 4. The overpressure in the large annular fluid inclusions at the time of decrepitation is estimated at around 80 MPa from the experiments of Leroy (1979) and Bodnar et al. (1989). Consequently, the first decrepitation of type 2 to give type 4 planes took place above 250° C where the corresponding isochores show a pressure difference of 80 MPa (Fig. 9A). The rotation of the stress field during the late history of the High Himalaya should be taken into account in any reconstruction. Further interpretation of the geometry of the stress field is not warranted, however, because of the poor constraints on the orientation of the sample. The water rich fluid inclusions (type 6) associated with the type 5 could result from unmixing of earlier H_2O-CO_2 rich fluids during decrepitation at very low pressure and temperature.

Conclusions

Using the geometry of microcracks and of fluid inclusions themselves, combined with microthermometric and compositional data, six different types of fluid inclusions were distinguished in a rock sample from the High Himalaya Sedimentary Series. One of these types shows annular inclusions; this shape is attributed to a confining pressure increase in a non-isotropic stress field. Two successive stress fields are deduced from the orientation of the inclusion planes relative to the schistosity. The bulk composition of the fluid is dominated by CO_2 (84 mol%) and H_2O. The chemical composition remains constant during the whole history of the sample indicating that it is buffered by the carbonate host rock and/or that one single fluid has been reworked in situ by decrepitation. Stable isotope studies on the fluids and on minerals show (1) that fluids were buffered by surrounding rocks for O and C and (2) that at least two types of water (metamorphic and meteoric) were involved. Finally, a (P, T, t, ε, σ) path is proposed for the sample, taking into account the northward tectonic denudation of the Himalaya inducing a short-lived tectonic burial below the Annapurna Range, and lastly, the rapid subsequent uplift. A 200 MPa increase in confining pressure has also been suggested by Hodges and Silverberg (1988) for the evolution of the hanging wall of the Main Central Thrust in Garhwal, further west. Are these two events related? This still remains an open question.

A post-trapping increase in density of high density CO_2 inclusions was first demonstrated by Olsen (1988) in natural samples in the Colorado Front Range. However, she could not clearly correlate this increase in density with any regional geological event. In the present paper, a (P, T, t, ε, σ) path of the HHSS is proposed and the increase of confining pressure attributed to a specific tectonic event.

As already demonstrated by Lespinasse and Pêcher (1986), Pêcher et al. (1985), de Alvarenga et al. (1990) and Cathelineau et al. (1990), it is possible to use fluid inclusions as structural markers. Inclusionists should now take into account the orientation and the textural analysis of the fluid inclusion planes combined with the more conventional microthermometric and isotopic studies, to be able to integrate the fluid history within the regional context, and possibly to recognize some events otherwise unobserved and for which there is no meso- or macro-scopic evidence either structural or metamorphic. Comparison of natural samples with the experimental results obtained by Pêcher (1981), Pêcher and Boullier (1984), Boullier et al. (1989) and Sterner and Bodnar (1989), provides a useful tool to integrate the fluid inclusion data in the (P, T, t, σ, ε) path of a metamorphic pile.

Acknowledgements. This work has been financed by the Institut National des Sciences de l'Univers (CNRS-INSU-DBT contribution 229, "Fluides Minéraux et cinétique"). The authors thank P. Le Fort for providing the NL 452 sample and geological orientations, and for interesting discussions, and A. Pêcher for allowing them to observe his experimental annular fluid inclusions. The interpretations given for the evolution of High Himalaya in this paper however are not the responsibility of these two colleagues. The authors are indebted to M. Pagel for indicating other examples of such inclusions in the literature. Fruitful discussions on fluids in Himalaya with Y. Gueguen, D. Jeannette, M. Rabinovich, B. Scaillet, S.M.F. Sheppard and J. Schott were highly appreciated. Constructive remarks by J. Henderson, M. Henderson, F. Robert, B. Taylor and J.M. Bertrand led to significant improvements of the manuscript, as well as a critical review by J. Touret. R. Lehmann and D. Mangin have brought an appreciated technical support. This paper is C.R.P.G. contribution n° 837 and CREGU contribution n° 220.

References

Alvarenga CJS de, Cathelineau M, Dubessy J (1990) Chronology and orientation of N_2-CH_4, CO_2-H_2O and H_2O-rich fluid inclusion trails in intrametamorphic quartz veins from the Cuiabà gold district, Brazil. Mineral Mag 54:245–255

Bakker RJ, Jansen BH (1990) Preferential water leakage from fluid inclusions by means of mobile dislocations. Nature 345:58–60

Barnes HL (1979) Geochemistry of hydrothermal ore deposits, 2nd edn. Wiley-Interscience, New York

Bodnar RJ, Bethke PM (1984) Systematics of stretching of fluid inclusions I: fluorite and sphalerite at 1 atmosphere confining pressure. Econ Geol 79:141–161

Bodnar RJ, Binns PR, Hall DL (1989) Synthetic fluid inclusions

– VI Quantitative evaluation of the decrepitation behaviour of fluid inclusions in quartz at one atmosphere confining pressure. J Metamorph Geol 7:229–242
Bordet P, Colchen M, Le Fort P, Pêcher A (1981) The geodynamic evolution of the Himalaya. Ten years of research in central Nepal Himalaya and some other regions. In: Gupta HK, Delany FM (eds) Zagros-Hindukush-Himalaya: geodynamic evolution. Am Geophys Union, Geodyn ser 3:149–168
Bottinga I (1968) Calculation of fractionation factors for carbon and oxygen exchange in the system calcite-carbon dioxide-water. J Phys Chem 72:800–808
Bottinga I, Javoy M (1973) Oxygen isotope partitioning among the minerals in igneous and metamorphic rocks. Rev Geophys Space Phys 13:401–418
Bouchez JL, Pêcher A (1981) Himalayan Main Central Thrust pile and its quartz-rich tectonites in Central Nepal. Tectonophysics 78:23–50
Boullier AM, Michot G, Pêcher A, Barres O (1989a) Diffusion and/or plastic deformation around fluid inclusions in synthetic quartz: new investigations. In: Bridgwater D (ed) Fluid movements, element transport and the composition of the crust. NATO ASI Series, Kluwer Pub group, Dordrecht, pp345–360
Boullier AM, Pêcher A, France-Lanord C (1989b) Fluid inclusions in the M.C.T. pile in Central Nepal. Terra abstracts 1:379–380
Brunel M, Kiénast JR (1986) Etude pétrostructurale des chevauchements ductiles himalayens sur la transversale de l'Everest-Makalu (Népal oriental). Can J Earth Sci 23:1117–1137
Burg JP, Brunel M, Gapais D, Chen GM, Liu GH (1984) Deformation of leucogranites of the crystalline Main Central Sheet in southern Tibet (China). J Struct Geol 6:535–542
Caby R, Pêcher A, Le Fort P (1983) Le grand chevauchement central himalayen: nouvelles données sur le métamorphisme inverse à la base de la Dalle du Tibet. Rev Géogr Phys Géol Dyn 24:89–100
Cathelineau M, Lespinasse M, Bastoul AM, Bernard C, Leroy J (1990) Fluid migration during contact metamorphism: the use of oriented fluid inclusion trails for a time/space reconstruction. Mineral Mag 54:169–182
Champenois M (1989) Interactive image analysis system: contribution to structural analysis, fluid inclusion studies and petrography. Terra abstracts 1:383
Clayton RN, Mayeda TK (1963) The use of bromine pentafluoride in the extraction of oxygen from oxides and silicates for isotopic analysis. Geochim Cosmochim Acta 27:43–52
Clayton RN, O'Neil JR, Mayeda TK (1972) Oxygen isotope fractionation between quartz and water. J Geophys Res 77:3057–3067
Colchen M, Le Fort P, Pêcher A (1986) Annapurna – Manaslu – Ganesh Himal. Notice de la carte géologique au 1/200000. Recherches géologiques dans l'Himalaya du Népal. Editions du CNRS, Paris
Craw D (1990) Fluid evolution during uplift of the Annapurna Himal, central Nepal. Lithos 24:137–150
Deniel C, Vidal P, Fernandez A, Le Fort P (1987) Isotopic study of the Manaslu granite (Himalaya, Nepal): inferences on the age and source of Himalayan leucogranites. Contrib Mineral Petrol 96:78–82
Dubessy J, Poty B, Ramboz C (1989) Advances in C–O–H–N–S fluid geochemistry based in micro-Raman spectrometric analysis of fluid inclusions. Eur J Mineral 1:517–534
Dubessy J, Scellen A-D, Claude J-M (1990) Geothermobarometry based on pyrrhotite composition and fluid inclusion studies: application to the scheelite-bearing deposit of Salau (Pyrénées, France). Eur J Mineral 2:235–243
France-Lanord C (1987) Chevauchement, métamorphisme et magmatisme en Himalaya du Népal Central. Etude isotopique H, C, O. Thesis, INPL Nancy
France-Lanord C, Sheppard SMF, Le Fort P (1988) Hydrogen and oxygen isotope variations in the High Himalaya peraluminous Manaslu leucogranite: evidence for heterogeneous sedimentary source. Geochim Cosmochim Acta 52:513–526
Friedman I (1953) Deuterium content of natural water and other substances. Geochim Cosmochim Acta 4:89–103
Gratier JP, Jenatton L (1984) Deformation by solution – deposition and reequilibration of fluid inclusions in crystals depending on temperature, internal pressure and stress. J Struct Geol 5:329–339
Herren E (1987) Zanskar shear zone: Northeast-southwest extension within the Higher Himalayas (Ladakh, India). Geology 15:409–413
Hodges KV, Silverberg DS (1988) Thermal evolution of the greater Himalaya, Garhwal, India. Tectonics 7:583–600
Hodges KV, Hubbard MS, Silverberg DS (1988) Metamorphic constraints on the thermal evolution of the central Himalayan orogen. Philos Trans R Soc London A 326:257–280
Hubbard MS (1989) Thermobarometric constraints on the thermal history of the Main Central Thrust Zone and Tibetan Slab, eastern Nepal Himalaya. J Metamorph Geol 7:19–30
Kerrick DM, Jacobs GK (1981) A modified Redlich-Kwong equation for H_2O, CO_2 and H_2O-CO_2 mixtures at elevated pressures and temperatures. Am J Sci 281:735–767
Krantz RL (1983) Microcracks in rocks: a review. Tectonophysics 100:449–480
Lapique F, Champenois M, Cheilletz A (1988) Un analyseur vidéographique interactif: descriptions et applications. Bull Minéral 111:679–687
Laubach SE (1989) Paleostress directions from the preferred orientation of closed microfractures (fluid inclusion planes) in sandstone, East Texas basin, U.S.A. J Struct Geol 11:603–611
Le Fort P (1975) Himalaya: the collided range. Present knowledge of the continental arc. Am J Sci 275A:1–44
Le Fort P (1981) Manaslu Leucogranite: A collision signature of the Himalaya. A model for its genesis and emplacement. J Geophys Res 86:10545–10568
Le Fort P (1989) The Himalayan orogenic segment. In: Sengör AMC (ed) Tectonic evolution of the Tethyan region, Klüwer Acad Pub, Dordrecht, pp289–386
Le Fort P, Pêcher A, Upreti BN (1987) A section through the Tibetan Slab in Central Nepal (Kali Gandaki valley): mineral chemistry and thermobarometry of the Main Central Thrust zone. In: Le Fort P, Colchen M, Montenat C (eds) Orogenic evolution of southern Asia (from Turkey to Indonesia), Sci Terre, Vol.47. Editions de la Fondation Scientifique de la Géologie et de ses applications, Nancy, pp 211–228
Lemmlein GC, Kliya MO (1954) Changes in fluid inclusions under the effect of temporary heating up a crystal (in Russian). Dokl Akad Nauk SSSR 94:233–236
Leroy J (1979) Contribution à l'étalonnage de la pression interne des inclusions fluides lors de leur décrépitation. Bull Minéral 102:584–593
Leroy J, Le Fort P, Poty B (1975) Some quartz crystals and their fluid inclusions from the Nepal Himalaya. Himalayan Geology, 5:139–152
Lespinasse M, Pêcher A (1986) Microfracturing and regional stress field: a study of the preferred orientations of fluid inclusion planes in a granite from the Massif Central, France. J Struct Geol 8:169–180
McCrea JM (1950) On the isotopic chemistry of carbonates and a palaeotemperature scale. J Chem Phys 18:849–857
Molnar P (1984) Structure and tectonics of the Himalaya: constraints and implications of geophysical data. Ann Rev Earth Planet Sci 12:489–518
Olsen SN (1988) High density CO_2 inclusions in the Colorado Front Range. Contrib Mineral Petrol 100:226–235
O'Neil JR, Clayton RN, Mayeda TK (1969) Oxygen isotope fractionation in divalent metal carbonates. J Chem Phys 51:5547–5558
Pagel M (1975) Cadre géologique des gisements d'uranium dans la structure Carswell (Saskatchewan, Canada). Thesis, Nancy
Pêcher A (1978) Déformation et métamorphisme associés à une zone de cisaillement, exemple du grand chevauchement hima-

layen (MCT), transversales des Annapurnas et du Manaslu, Népal. Thesis, Grenoble

Pêcher A (1979) Les inclusions fluides des quartz d'exsudation de la zone du MCT himalayen au Népal Central: données sur la phase fluide dans une grade zone de cisaillement crustal. Bull Minéral 102:537–554

Pêcher A (1981) Experimental decrepitation and reequilibration of fluid inclusions in synthetic quartz. Tectonophysics 78:567–584

Pêcher A (1989) The metamorphism in the Central Himalaya. J Metamorph Geol 7:31–41

Pêcher A, Boullier AM (1984) Evolution à pression et température élevées d'inclusions fluides dans un quartz synthétique. Bull Minéral 107:139–153

Pêcher A, Scaillet B (1989) La structure du Haut-Himalaya au Garhwal (Indes). Eclogae Geol Helv 82:655–668

Pêcher A, Le Fort P (1986) The metamorphism in Central Himalaya, its relations with the thrust tectonic. In: Le Fort P, Colchen M and Montenat C (eds) Orogenic evolution of southern Asia (from Turkey to Indonesia), Sci Terre, Vol. 47. Editions de la Fondation de la Géologie et de ses applications. Nancy, pp 285–309

Pêcher A, Lespinasse M, Leroy J (1985) Relations between fluid inclusions trails and regional stress field: a tool for fluid chronology. Lithos 18:229–327

Poty B, Leroy J, Jachimowicz L (1976) Un nouvel appareil pour la mesure des températures sous le microscope: l'installation de microthermométrie Chaix Méca. Bull Soc Fr Minéral Cristallogr 99:182–186

Ramboz C, Schnapper D, Dubessy J (1985) The P-V-T-X-f (O_2) evolution of $H_2O-CO_2-CH_4$-bearing fluid in a wolframite vein. Reconstructions from fluid inclusion studies. Geochim Cosmochim Acta 49:205–219

Roedder E (1984) Fluid inclusions (Reviews in Mineralogy vol 12). Mineralogical Society of America, Washington DC

Roedder E (1981) Origin of fluid inclusions and changes that occur after trapping. In: Hollister LS, Crawford ML (eds) Fluid inclusions: applications to petrology (Short Course Handbook 6). Mineralogical Association of Canada, Calgary, pp 101–137

Sabouraud C (1981) Décrépitation expérimentale d'inclusions sous pression. Application au cas d'inclusions primaires de fluorine. C R Acad Sci 292:729–732

Safronov GM (1965) On the morphology of liquid inclusions in crystals of quartz from Pamir. In: Yermakov NP (ed) Research on the nature of mineral-forming solutions. Pergamon, Oxford, pp 531–535

Sauniac S, Touret J (1983) Petrology and fluid inclusions of a quartz-kyanite segregation in the main thrust zone of the Himalayas. Lithos 16:35–45

Smith DL, Evans B (1984) Diffusional crack healing in quartz. J Geophys Res 89:4125–4135

Sterner SM, Bodnar RJ (1989) Synthetic fluid inclusions. VII: Reequilibration of fluid inclusions in quartz during laboratory-simulated metamorphic burial and uplift. J Metamorph Geol 7:243–260

Suzuoki T, Epstein S (1976) Hydrogen isotope fractionation between OH-bearing minerals and water. Geochim Cosmochim Acta 40:1229–1240

Toulmin P III, Barton PB (1964) A thermodynamic study of pyrite and pyrrhotite. Geochim Cosmochim Acta 28:641–671

Touret J (1977) The significance of fluid inclusions in metamorphic rocks. In: Fraser DG (ed) Thermodynamics in Geology. D Reidel Publ Co, Dordrecht, pp 203–227

Touret J (1981) Fluid inclusions in high-grade metamorphic rocks. In: Hollister LS, Crawford ML (eds) Fluid inclusions: applications to petrology (Short Course Handbook 6). Mineralogical Association of Canada, Calgary, pp 182–208

Tullis JA, Christie JM, Griggs DT (1973) Microstructures and preferred orientation of experimentally deformed quartzites. Geol Soc Am Bull 84:297–314

Tuttle OF (1949) Structural petrology of planes of liquid inclusions. J Geol 57:331–356

Ulrich MR, Bodnar RJ (1988) Systematics of stretching of fluid inclusions II: barite at 1 atm confining pressure. Econ Geol 83:1037–1046

Urai JL (1983) Deformation of wet salt rocks. Thesis, University of Utrecht

Zhang YG (1988) Détermination expérimentale des propriétés P-V-T-X de systèmes fluides géochimiquement réalistes par la méthode des inclusions synthétiques: domaines homogènes et immiscibilité. Thesis, INPL Nancy

Editorial responsibility: J. Touret